

# Tidal deformability of neutron stars with realistic equations of state and their gravitational wave signatures in binary inspiral

Tanja Hinderer<sup>1</sup>, Benjamin D. Lackey<sup>2</sup>, Ryan N. Lang<sup>3,4</sup>, Jocelyn S. Read<sup>5</sup>

<sup>1</sup>*Theoretical Astrophysics, California Institute of Technology, Pasadena, CA 91125, USA*

<sup>2</sup>*Department of Physics, University of Wisconsin-Milwaukee, P.O. Box 413, Milwaukee, WI 53201, USA*

<sup>3</sup>*Department of Physics and MIT Kavli Institute, MIT,  
77 Massachusetts Avenue, Cambridge, MA 02139, USA*

<sup>4</sup>*Gravitational Astrophysics Laboratory, NASA Goddard Space Flight Center, 8800 Greenbelt Rd., Greenbelt, MD 20771, USA*

<sup>5</sup>*Max-Planck-Institut für Gravitationsphysik Albert-Einstein-Institut, Am Mühlenberg 1, 14476 Potsdam, Germany*

The early part of the gravitational wave signal of binary neutron star inspirals can potentially yield robust information on the nuclear equation of state. The influence of a star's internal structure on the waveform is characterized by a single parameter: the tidal deformability  $\lambda$ , which measures the star's quadrupole deformation in response to the companion's perturbing tidal field. We calculate  $\lambda$  for a wide range of equations of state and find that the value of  $\lambda$  spans an order of magnitude for the range of equation of state models considered.

An analysis of the feasibility of discriminating between neutron star equations of state with gravitational wave observations of the early part of the inspiral reveals that the measurement error in  $\lambda$  increases steeply with the total mass of the binary. Comparing the errors with the expected range of  $\lambda$ , we find that Advanced LIGO observations of binaries at a distance of 100 Mpc will probe only unusually stiff equations of state, while the proposed Einstein Telescope is likely to see a clean tidal signature.

PACS numbers: 04.40.Dg, 26.60.Kp, 97.60.Jd, 95.85.Sz

## I. INTRODUCTION AND SUMMARY

The observation of inspiraling binary neutron stars (NSs) with ground-based gravitational-wave detectors such as LIGO and Virgo may provide significantly more information about neutron-star structure, and the highly uncertain equation of state (EOS) of neutron-star matter, than is currently available. The available electromagnetic observations of neutron stars provide weak constraints from properties such as the star's mass, spin, and gravitational redshift (see for example [1, 2]). Simultaneous measurements of both the mass and radius of a neutron star [3, 4, 5, 6, 7], on the other hand, have the potential to make significantly stronger constraints. These measurements, however, depend on detailed modeling of the radiation mechanisms at the neutron-star surface and absorption in the interstellar medium, and are subject to systematic uncertainties.

Another possibility for obtaining information about the neutron star EOS is from the inspiral of binary neutron stars due to gravitational radiation. The tidal distortion of neutron stars in a binary system links the EOS describing neutron-star matter to the gravitational-wave emission during the inspiral. Initial estimates showed that for LIGO, tidal effects change the phase evolution only at the end of inspiral, and that point particle post-Newtonian waveforms can be used for template-based detection [8, 9, 10]. With the projected sensitivities of later-generation detectors, however, effects which can be neglected for the purpose of detection may become measurable in the strongest observed signals.

While EOS effects are largest during the late inspiral and merger of two neutron stars where numerical sim-

ulations must be used to predict the signal, Flanagan and Hinderer showed that a small but clean tidal signature arises in the inspiral below 400 Hz [11]. This signature amounts to a phase correction which can be described in terms of a single EOS-dependent tidal deformability parameter  $\lambda$ , namely the ratio of each star's induced quadrupole to the tidal field of its companion. The parameter  $\lambda$  depends on the EOS via both the NS radius  $R$  and a dimensionless quantity  $k_2$ , called the Love number [12, 13, 14]:  $\lambda = 2/(3G)k_2R^5$ .

The relativistic Love numbers of polytropic<sup>1</sup> EOS were examined first by Flanagan and Hinderer [11, 15] and later by others in more detail [16, 17]. Flanagan and Hinderer also examined the measurability of the tidal deformability of polytropes and suggested that Advanced LIGO could start to place interesting constraints on  $\lambda$  for nearby events. However, they used incorrect values for  $k_2$ , which overestimated  $\lambda$  by a factor of  $\sim 2 - 3$  and were therefore overly optimistic about the potential measurability. In addition, polytropes are known to be a poor approximation to the neutron star equation of state, and there may be significant differences in the tidal

---

<sup>1</sup> Polytropes are often written in two forms. The first form is expressed as  $p = K\epsilon^{1+1/n}$ , where  $p$  is the pressure,  $\epsilon$  is the energy density,  $K$  is a pressure constant, and  $n$  is the polytropic index. The second form, is given by  $p = K\rho^{1+1/n}$ , where  $\rho$  is the rest-mass density, defined as the baryon number density times the baryon rest mass. The first form was mainly used in the recent papers [15, 16, 17]. However, the second form is more commonly used in the neutron-star literature and is more closely tied to the thermodynamics of a Fermi gas. We will use both forms as was done in Ref. [16].

deformability between polytropes and “realistic” EOS. In this paper, we calculate the deformability for realistic EOS, and show that a tidal signature is actually only marginally detectable with Advanced LIGO.

In Sec. II we describe how the Love number and tidal deformability can be calculated for tabulated EOS. We use the equations for  $k_2$  developed in [15], which arise from a linear perturbation of the Oppenheimer-Volkoff (OV) equations of hydrostatic equilibrium. In Sec. III we then calculate  $k_2$  and  $\lambda$  as a function of mass for several EOS commonly found in the literature. We find that, in contrast to the Love number, the tidal deformability has a wide range of values, spanning roughly an order of magnitude over the observed mass range of neutron stars in binary systems.

As discussed above, the direct practical importance of the stars’ tidal deformability for gravitational wave observations of NS binary inspirals is that it encodes the EOS influence on the waveform’s phase evolution during the early portion of the signal, where it is accurately modeled by post-Newtonian (PN) methods. In this regime, the influence of tidal effects is only a small correction to the point-mass dynamics. However, when the signal is integrated against a theoretical waveform template over many cycles, even a small contribution to the phase evolution can be detected and could give information about the NS structure.

Following [11], we calculate in Sec. IV the measurability of the tidal deformability for a wide range of equal- and unequal- mass binaries, covering the entire expected range of NS masses and EOS, and with proposed detector sensitivity curves for second- and third- generation detectors. We show that the measurability of  $\lambda$  is quite sensitive to the total mass of the system, with very low-mass neutron stars contributing significant phase corrections that are optimistically detectable in Advanced LIGO, while larger-mass neutron stars are more difficult to distinguish from the  $k_2 = 0$  case of black holes [16, 17]. In third-generation detectors, however, the tenfold increase in sensitivity allows a finer discrimination between equations of state leading to potential measurability of a large portion of proposed EOSs over most of the expected neutron star mass range.

We conclude by briefly considering how the errors could be improved with a more careful analysis of the detectors and extension of the understanding of EOS effects to higher frequencies.

Finally, in the Appendix we compute the leading order EOS-dependent corrections to our model of the tidal effect and derive explicit expressions for the resulting corrections to the waveform’s phase evolution, extending the analysis of Ref. [11]. Estimates of the size of the phase corrections show that the main source of error are post-1 Newtonian corrections to the Newtonian tidal effect itself, which are approximately twice as large as other, EOS-dependent corrections at a frequency of 450 Hz. Since these point-particle corrections do not depend on unknown NS physics, they can easily be incorporated into

the analysis. A derivation of the explicit post-Newtonian correction terms is the subject of Ref. [18].

*Conventions:* We set  $G = c = 1$ .

## II. CALCULATION OF THE LOVE NUMBER AND TIDAL DEFORMABILITY

As in [11] and [15], we consider a static, spherically symmetric star, placed in a static external quadrupolar tidal field  $\mathcal{E}_{ij}$ . To linear order, we define the tidal deformability  $\lambda$  relating the star’s induced quadrupole moment  $Q_{ij}$  to the external tidal field,

$$Q_{ij} = -\lambda \mathcal{E}_{ij}. \quad (1)$$

The coefficient  $\lambda$  is related to the  $l = 2$  dimensionless tidal Love number  $k_2$  by

$$k_2 = \frac{3}{2} \lambda R^{-5}. \quad (2)$$

The star’s quadrupole moment  $Q_{ij}$  and the external tidal field  $\mathcal{E}_{ij}$  are defined to be coefficients in an asymptotic expansion of the total metric at large distances  $r$  from the star. This expansion includes, for the metric component  $g_{tt}$  in asymptotically Cartesian, mass-centered coordinates, the standard gravitational potential  $m/r$ , plus two leading order terms arising from the perturbation, one describing an external tidal field growing with  $r^2$  and one describing the resulting tidal distortion decaying with  $r^{-3}$ :

$$-\frac{(1 + g_{tt})}{2} = -\frac{m}{r} - \frac{3Q_{ij}}{2r^3} n^i n^j + \dots + \frac{\mathcal{E}_{ij}}{2} r^2 n^i n^j + \dots, \quad (3)$$

where  $n^i = x^i/r$  and  $Q_{ij}$  and  $\mathcal{E}_{ij}$  are both symmetric and traceless. The relative size of these multipole components of the perturbed spacetime gives the constant  $\lambda$  relating the quadrupole deformation to the external tidal field as in Eq. (1).

To compute the metric (3), we use the method discussed in [15]. We consider the problem of a linear static perturbation expanded in spherical harmonics following [19]. Without loss of generality we can set the azimuthal number  $m = 0$ , as the tidal deformation will be axisymmetric around the line connecting the two stars which we take as the axis for the spherical harmonic decomposition. Since we will be interested in applications to the early stage of binary inspirals, we will also specialize to the leading order for tidal effects,  $l = 2$ .

Introducing a linear  $l = 2$  perturbation onto the spherically symmetric star results in a static (zero-frequency), even-parity perturbation of the metric, which in the Regge-Wheeler gauge [20] can be simplified [15] to give

$$ds^2 = -e^{2\Phi(r)} [1 + H(r)Y_{20}(\theta, \varphi)] dt^2 + e^{2\Lambda(r)} [1 - H(r)Y_{20}(\theta, \varphi)] dr^2 + r^2 [1 - K(r)Y_{20}(\theta, \varphi)] (d\theta^2 + \sin^2 \theta d\varphi^2), \quad (4)$$

where  $K(r)$  is related to  $H(r)$  by  $K'(r) = H'(r) + 2H(r)\Phi'(r)$ . Here primes denote derivatives with respect to  $r$ . The corresponding perturbations of the perfect fluid stress-energy tensor components are  $\delta T_0^0 = -\delta\epsilon(r)Y_{20}(\theta, \varphi)$  and  $\delta T_i^i = \delta p(r)Y_{20}(\theta, \varphi)$ , where  $\epsilon$  is the energy density and  $p$  the pressure. The function  $H(r)$  satisfies the differential equation

$$\begin{aligned} & \left( -\frac{6e^{2\Lambda}}{r^2} - 2(\Phi')^2 + 2\Phi'' + \frac{3}{r}\Lambda' \right. \\ & \left. + \frac{7}{r}\Phi' - 2\Phi'\Lambda' + \frac{f}{r}(\Phi' + \Lambda') \right) H \\ & + \left( \frac{2}{r} + \Phi' - \Lambda' \right) H' + H'' = 0. \end{aligned} \quad (5)$$

Here  $f$  is given by

$$\delta\epsilon = f\delta p \quad (6)$$

which for slow changes in matter configurations corresponds to  $f = d\epsilon/dp$ .

The method of calculating the tidal perturbation for a general equation of state table is similar to the method of calculating moment of inertia in the slow rotation approximation [21]. The specific implementation we use follows the moment of inertia calculation in Appendix A of [2], via an augmentation of the OV system of equations<sup>2</sup>:

$$e^{2\Lambda} = \left( 1 - \frac{2m_r}{r} \right)^{-1}, \quad (7)$$

$$\frac{d\Phi}{dr} = -\frac{1}{\epsilon + p} \frac{dp}{dr}, \quad (8)$$

$$\frac{dp}{dr} = -(\epsilon + p) \frac{m_r + 4\pi r^3 p}{r(r - 2m_r)}, \quad (9)$$

$$\frac{dm_r}{dr} = 4\pi r^2 \epsilon. \quad (10)$$

The second-order differential equation for  $H$  is separated into a first-order system of ODEs in terms of the usual OV quantities  $m_r$ ,  $p(r)$ , and  $\epsilon(p)$ , as well as the additional functions  $H(r)$ ,  $\beta(r) = dH/dr$ , and the equation

of state function  $f(p)$  (recall  $f = d\epsilon/dp$ ):

$$\begin{aligned} \frac{dH}{dr} &= \beta \\ \frac{d\beta}{dr} &= 2 \left( 1 - 2\frac{m_r}{r} \right)^{-1} H \left\{ -2\pi [5\epsilon + 9p + f(\epsilon + p)] \right. \\ & \quad \left. + \frac{3}{r^2} + 2 \left( 1 - 2\frac{m_r}{r} \right)^{-1} \left( \frac{m_r}{r^2} + 4\pi r p \right)^2 \right\} \\ & \quad + \frac{2\beta}{r} \left( 1 - 2\frac{m_r}{r} \right)^{-1} \left\{ -1 + \frac{m_r}{r} + 2\pi r^2 (\epsilon - p) \right\}. \end{aligned} \quad (11)$$

These are combined with Eqs. (7)–(10), and the augmented system is solved simultaneously. The system is integrated outward starting just outside the center using the expansions  $H(r) = a_0 r^2$  and  $\beta(r) = 2a_0 r$  as  $r \rightarrow 0$ . The constant  $a_0$  determines how much the star is deformed and can be chosen arbitrarily as it cancels in the expression for the Love number. The ODE for  $H(r)$  outside the star, where  $T_{\mu\nu} = 0$ , has a general solution in terms of associated Legendre functions  $Q_2^2(r/m - 1) \sim r^{-3}$  at large  $r$ , and  $P_2^2(r/m - 1) \sim r^2$  at large  $r$ . The boundary conditions that determine the unique choice of this solution follow from matching the interior and exterior solutions and their first derivatives at the boundary of the star, where  $r = R$ . By comparison with Eq. (3), the coefficients of the external solution can then be identified with the axisymmetric tidal field and quadrupole moment via  $\mathcal{E}Y_{20}(\theta, \varphi) = \mathcal{E}_{ij}n^i n^j$ , and  $QY_{20}(\theta, \varphi) = Q_{ij}n^i n^j = -\lambda \mathcal{E}_{ij}n^i n^j$  as was done in [15]. Here,  $\mathcal{E}$  and  $Q$  are the magnitudes of the  $l = 2$ ,  $m = 0$  spherical harmonic coefficients of the tidal tensor and quadrupole moment respectively.

Defining the quantity

$$y = \frac{R\beta(R)}{H(R)} \quad (13)$$

for the internal solution, the  $l = 2$  Love number is

$$\begin{aligned} k_2 &= \frac{8C^5}{5} (1 - 2C)^2 [2 + 2C(y - 1) - y] \\ & \quad \times \left\{ 2C[6 - 3y + 3C(5y - 8)] \right. \\ & \quad \left. + 4C^3[13 - 11y + C(3y - 2) + 2C^2(1 + y)] \right. \\ & \quad \left. + 3(1 - 2C)^2 [2 - y + 2C(y - 1)] \ln(1 - 2C) \right\}^{-1}, \end{aligned} \quad (14)$$

where  $C = m/R$  is the compactness of the star.

For stars with a nonzero density at the surface (for example strange quark matter or an incompressible  $n = 0$  polytrope), the term  $(f/r)(\Phi' + \Lambda')$  in Eq. (5) blows up at the surface  $r = R$  and  $H'(r)$  is no longer continuous across the surface. Following the discussion in [22] for

<sup>2</sup> Here we present the equations in terms of the radial coordinate  $r$ ; the extension to the enthalpy variable  $\eta$  used in [2] is straightforward.

<sup>3</sup> We use  $m_r$  for the mass enclosed within radius  $r$  instead of  $m(r)$  to avoid confusion with the total mass of the star, which we will label  $m$ .

an  $n = 0$  polytrope, this discontinuity leads to an extra term in the expression above for  $y$ :

$$y = \frac{R\beta(R)}{H(R)} - \frac{4\pi R^3 \epsilon_-}{m} \quad (15)$$

where  $\epsilon_-$  is the density just inside the surface.

### III. LOVE NUMBERS AND TIDAL DEFORMABILITIES FOR CANDIDATE EOS

Differences between candidate EOS can have a significant effect on the tidal interactions of neutron stars. In this paper we consider a sample of EOS from Refs. [2, 23] with a variety of generation methods and particle species. The sample is chosen to include EOS with the largest range of behaviors for  $k_2(m/R)$ ,  $k_2(m)$  and  $\lambda(m)$  rather than to fairly represent the different generation methods. We also restrict ourselves to stars with a maximum mass greater than  $1.5 M_\odot$ , which is conservatively low given recent neutron-star mass observations [24, 25, 26, 27, 28]. We consider 7 EOS with just normal  $npe\mu$  matter (SLY [29], AP1 and AP3 [30], FPS [31], MPA1 [32], MS1 and MS2 [33]), 8 EOS that also incorporate some combination of hyperons, pion condensates, and quarks (PS [34], BGN1H1 [35], GNH3 [36], H1 and H4 [37], PCL2 [38], ALF1 and ALF2 [39]), and 3 self-bound strange quark matter EOS (SQM1-3 [40]). A brief description of these EOS and their properties can be found in [2, 23].

The generic behavior of the Love number  $k_2$  is shown in the top panel of Fig. 1 as a function of compactness  $m/R$  for different types of EOS. The two types of polytropes, energy and rest-mass density polytropes, are shown in gray. They coincide in the limit  $m/R \rightarrow 0$  where  $\epsilon \rightarrow \rho$  as the star's density goes to zero, and in the limit  $n \rightarrow 0$  where  $\epsilon(p)$  and  $\rho(p)$  are both constant. This can be seen from the first law of thermodynamics,

$$d\frac{\epsilon}{\rho} = -pd\frac{1}{\rho}, \quad (16)$$

which relates  $\epsilon$  to  $\rho$ .

The sequences labeled ‘‘Normal’’ correspond to the 15 EOS with a standard nuclear matter crust, and the 3 sequences labeled ‘‘SQM’’ correspond to the crustless EOS SQM1-3 where the pressure is zero below a few times nuclear density. Within these two classes, there is little variation in behavior, so we do not explicitly label each candidate EOS.

The bottom panel of Fig. 1 shows  $k_2(m)$  for the realistic EOS, which is more astrophysically relevant because mass, not compactness, is the measurable quantity during binary inspiral. Unlike the quantity  $k_2(m/R)$ ,  $k_2(m)$  depends on the constant  $K$  for polytropes, so polytropic EOS are not shown. There is more variation in  $k_2$  for fixed mass than for fixed compactness.

The behavior of these curves can be understood as follows: The Love number  $k_2$  measures how easily the bulk

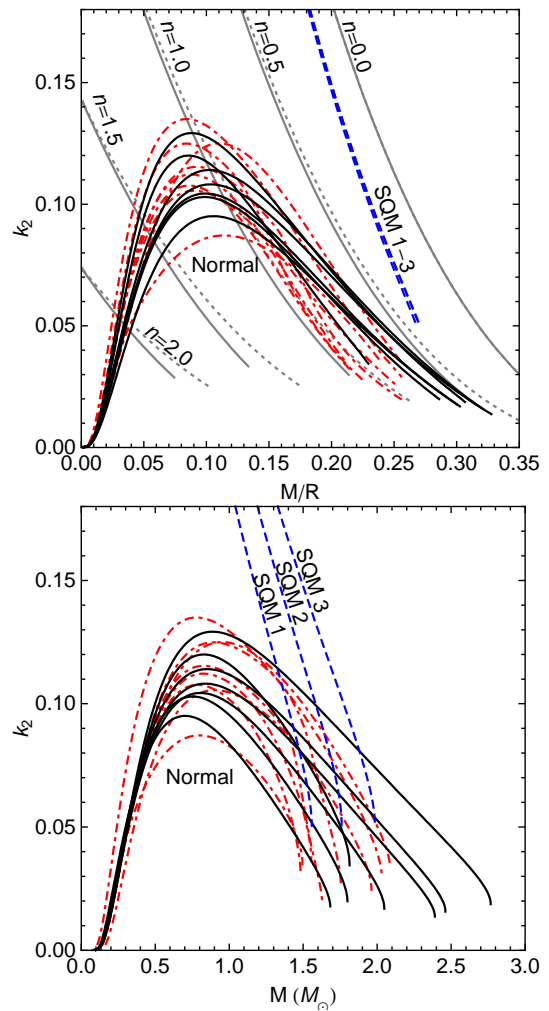


FIG. 1: Top panel: Love number as a function of compactness. Gray dotted curves are energy density polytropes ( $p = K\epsilon^{1+1/n}$ ), and gray solid curves are rest-mass density polytropes ( $p = K\rho^{1+1/n}$ ). Both polytropes are the same for  $n = 0$ . EOS with only  $npe\mu$  matter are solid and those that also incorporate  $\pi$ /hyperon/quark matter are dot-dashed. The three SQM EOS are dashed and overlap. They approach the  $n = 0$  curve at low compactness, where  $k_2$  has a maximum value of 0.75 as  $m/R \rightarrow 0$ . Bottom panel: Love number as a function of mass for the same set of realistic EOS. Note that there is more variation in  $k_2$  between different EOS for fixed mass than for fixed compactness.

of the matter in a star is deformed. If most of the star's mass is concentrated at the center (centrally condensed), the tidal deformation will be smaller. For polytropes, matter with a higher polytropic index  $n$  is softer and more compressible, so these polytropes are more centrally condensed. As a result,  $k_2$  decreases as  $n$  increases. The limiting case  $n = 0$  represents a uniform density star and has the largest Love number possible. The Love number also decreases with increasing compactness, and from Eq. (14) it can be seen that  $k_2$  vanishes at the compact-

ness of a black hole ( $m/R = 0.5$ ) regardless of the EOS dependent quantity  $y$  [16, 17].

Normal matter EOS behave approximately as polytropes for large compactness. However, for smaller compactness, the softer crust becomes a greater fraction of the star, so the star is more centrally condensed and  $k_2$  smaller. For strange quark matter, the EOS is extremely stiff near the minimum density, and the star behaves approximately as an  $n = 0$  polytrope for small compactness. As the central density and compactness increase, the softer part of the EOS has a larger effect, and the star becomes more centrally condensed.

The parameter that is directly measurable by gravitational wave observations of a binary neutron star inspiral is proportional to the tidal deformability  $\lambda$ , which is shown for each candidate EOS in Fig. 2. The values of  $\lambda$  for the candidate EOS show a much wider range of behaviors than for  $k_2$  because  $\lambda$  is proportional to  $k_2 R^5$ , and the candidate EOS produce a wide range of radii (9.4–15.5 km for a  $1.4 M_\odot$  star for normal EOS and 8.9–10.9 km for the SQM EOS). See Table I.

TABLE I: Properties of a  $1.4 M_\odot$  neutron star for the 18 EOS discussed in the text.

EOS	$R(\text{km})$	$m/R$	$k_2$	$\lambda(10^{36} \text{ g cm}^2 \text{ s}^2)$
SLY	11.74	0.176	0.0763	1.70
AP1	9.36	0.221	0.0512	0.368
AP3	12.09	0.171	0.0858	2.22
FPS	10.85	0.191	0.0663	1.00
MPA1	12.47	0.166	0.0924	2.79
MS1	14.92	0.139	0.110	8.15
MS2	13.71	0.151	0.0883	4.28
PS	15.47	0.134	0.104	9.19
BGN1H1	12.90	0.160	0.0868	3.10
GNH3	14.20	0.146	0.0867	5.01
H1	12.86	0.161	0.0738	2.59
H4	13.76	0.150	0.104	5.13
PCL2	11.76	0.176	0.0577	1.30
ALF1	9.90	0.209	0.0541	0.513
ALF2	13.19	0.157	0.107	4.28
SQM1	8.86	0.233	0.098	0.536
SQM2	10.03	0.206	0.136	1.38
SQM3	10.87	0.190	0.166	2.52

For normal matter,  $\lambda$  becomes large for stars near the minimum mass configuration at roughly  $0.1 M_\odot$  because they have a large radius. For masses in the expected mass range for binary inspirals, there are several differences between EOS with only  $npe\mu$  matter and those with condensates. EOS with condensates have, on average, a larger  $\lambda$ , primarily because they have, on average, larger radii. The quark hybrid EOS ALF1 with a small radius (9.9 km for a  $1.4 M_\odot$  star) and the nuclear matter

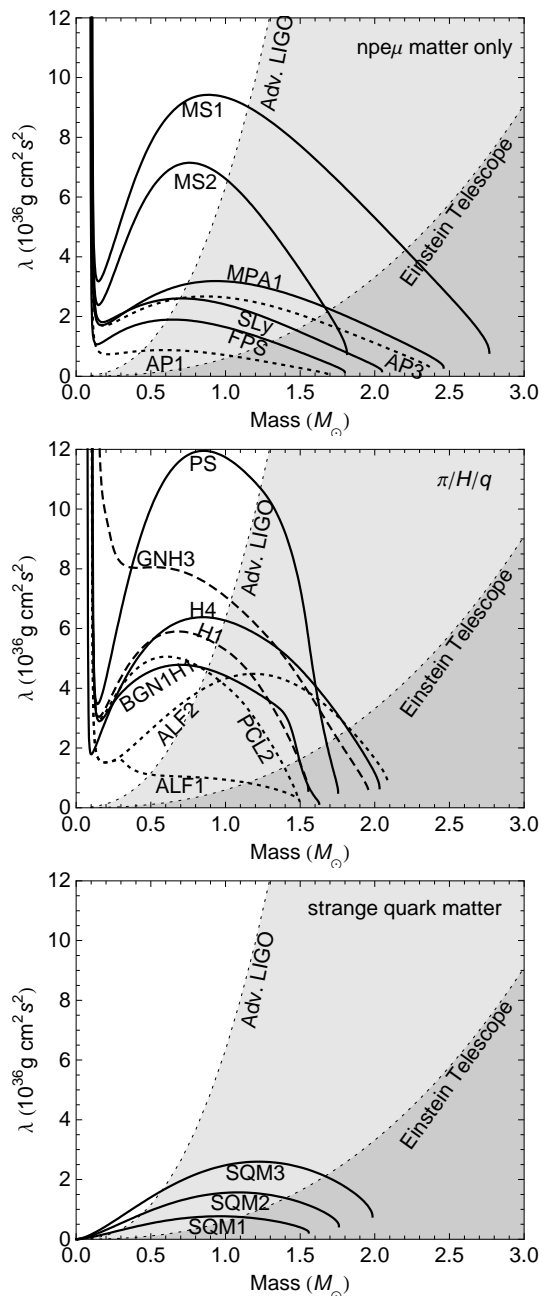


FIG. 2: Tidal deformability  $\lambda$  of a single neutron star as a function of neutron-star mass for a range of realistic EOS. The top figure shows EOS that only include  $npe\mu$  matter; the middle figure shows EOS that also incorporate  $\pi$ /hyperon/quark matter; the bottom figure shows strange quark matter EOS. The dashed lines between the various shaded regions represent the expected uncertainties in measuring  $\lambda$  for an equal-mass binary inspiral at a distance of  $D = 100$  Mpc as it passes through the gravitational wave frequency range 10 Hz–450 Hz. Observations with Advanced LIGO will be sensitive to  $\lambda$  in the unshaded region, while the Einstein Telescope will be able to measure  $\lambda$  in the unshaded and light shaded regions. See text below.

only EOSs MS1 and MS2 with large radii (14.9 km and 14.5 km, respectively, at  $1.4 M_\odot$ ) are exceptions to this trend.

For strange quark matter stars, there is no minimum mass, so the radius (and therefore  $\lambda$ ) approaches zero as the mass approaches zero. At larger masses, the tidal deformability of SQM stars remains smaller than most normal matter stars because, despite having large Love numbers, the radii of SQM stars are typically smaller.

Error estimates  $\Delta\lambda$  for an equal-mass binary inspiral at 100 Mpc are also shown in Fig. 2 for both Advanced LIGO and the Einstein Telescope. They will be discussed in the next section.

#### IV. MEASURING EFFECTS ON GRAVITATIONAL RADIATION

We wish to calculate the contribution from realistic tidal effects to the phase evolution and resulting gravitational wave spectrum of an inspiraling neutron star binary. In the secular limit, where the orbital period is much shorter than the gravitational radiation reaction timescale, we consider the tidal contribution to the energy  $E$  and energy flux  $dE/dt$  for a quasi-circular inspiral using the formalism developed by Flanagan and Hinderer [11], which adds the following leading-order terms to the post-Newtonian point-particle corrections (PN-PP corr.):

$$E(x) = -\frac{1}{2}M\eta x \left[ 1 + (\text{PN-PP corr.}) - 9\frac{m_2}{m_1} \frac{\lambda_1}{M^5} x^5 + 1 \leftrightarrow 2 \right], \quad (17)$$

$$\dot{E}(x) = -\frac{32}{5}\eta^2 x^5 \left[ 1 + (\text{PN-PP corr.}) + 6\frac{m_1 + 3m_2}{m_1} \frac{\lambda_1}{M^5} x^5 + 1 \leftrightarrow 2 \right]. \quad (18)$$

Here  $\lambda_1 = \lambda(m_1)$  and  $\lambda_2 = \lambda(m_2)$  are the tidal deformabilities of stars 1 and 2, respectively.  $M = m_1 + m_2$  is the total mass,  $\eta = m_1 m_2 / M^2$  is the dimensionless reduced mass, and  $x$  is the post-Newtonian dimensionless parameter given by  $x = (\omega M)^{2/3}$ , where  $\omega$  is the orbital angular frequency. One can then use

$$dx/dt = \frac{\dot{E}}{dE/dx} \quad (19)$$

to estimate the evolution of the quadrupole gravitational wave phase  $\Phi$  via  $d\Phi/dt = 2\omega = 2x^{3/2}/M$ .

Each equation of state gives in this approximation a known phase contribution as a function of  $m_1$  and  $m_2$ , or as a function of the total mass  $M = m_1 + m_2$  and the mass ratio  $m_2/m_1$ , via  $\lambda(m_1)$  and  $\lambda(m_2)$  for that EOS. Although we calculated  $\lambda$  for individual neutron stars, the universality of the neutron star core equation of state allows us to predict the tidal phase contribution

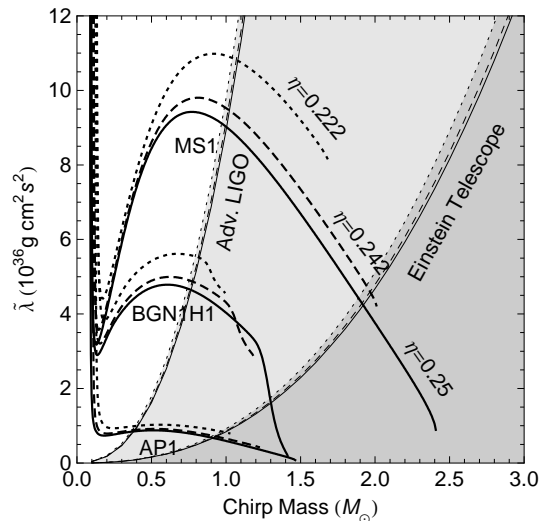


FIG. 3: Weighted  $\tilde{\lambda}$  for a range of chirp mass  $\mathcal{M}$  and dimensionless reduced mass  $\eta$ , for three of the EOSs considered above. The values of  $\eta$  equal to  $\{0.25, 0.242, 0.222\}$  correspond to the mass ratios  $m_2/m_1 = \{1.0, 0.7, 0.5\}$ . Also plotted (as in Fig. 2) are the uncertainties  $\Delta\tilde{\lambda}$  in measuring  $\tilde{\lambda}$  for a binary at 100 Mpc between 10 Hz–450 Hz. The solid, dashed, and dotted curves correspond to  $\Delta\tilde{\lambda}$  for  $\eta = 0.25$ , 0.242, and 0.222 respectively.

for a given binary system from each EOS. Following [11], we discuss the constraint on the weighted average

$$\tilde{\lambda} = \frac{1}{26} \left[ \frac{m_1 + 12m_2}{m_1} \lambda(m_1) + \frac{m_2 + 12m_1}{m_2} \lambda(m_2) \right], \quad (20)$$

which reduces to  $\lambda$  in the equal mass case. The contribution to  $d\Phi/dx$  from the tidal deformation, which adds linearly to the known PP phase evolution, is

$$\left. \frac{d\Phi}{dx} \right|_T = -\frac{195}{8} \frac{x^{3/2} \tilde{\lambda}}{M^5 \eta}. \quad (21)$$

The weighted average  $\tilde{\lambda}$  is plotted as a function of chirp mass  $\mathcal{M} = (m_1 m_2)^{3/5} / M^{1/5}$  in Fig. 3 for three of the EOS and for three values of  $\eta$ : equal mass ( $\eta = 0.25$ ), large but plausible mass ratio [41] ( $\eta = 0.242$ ), and extremely large mass ratio ( $\eta = 0.222$ ).

We can determine the significance of the tidal effect on gravitational waveforms in a given frequency range by considering the resulting change in phase accumulated as a function of frequency. In the case of template-based searches, for example, a drift in phase of half a cycle leads to destructive interference between the signal and template, halting the accumulation of signal to noise ratio. The phase contributions to binary neutron stars of various masses from a range of realistic tidal deformabilities are plotted in Fig. 4.

The post-Newtonian formalism itself is sensitive to high-order corrections at the frequencies at which the tidal effect becomes significant; as reference, we show in

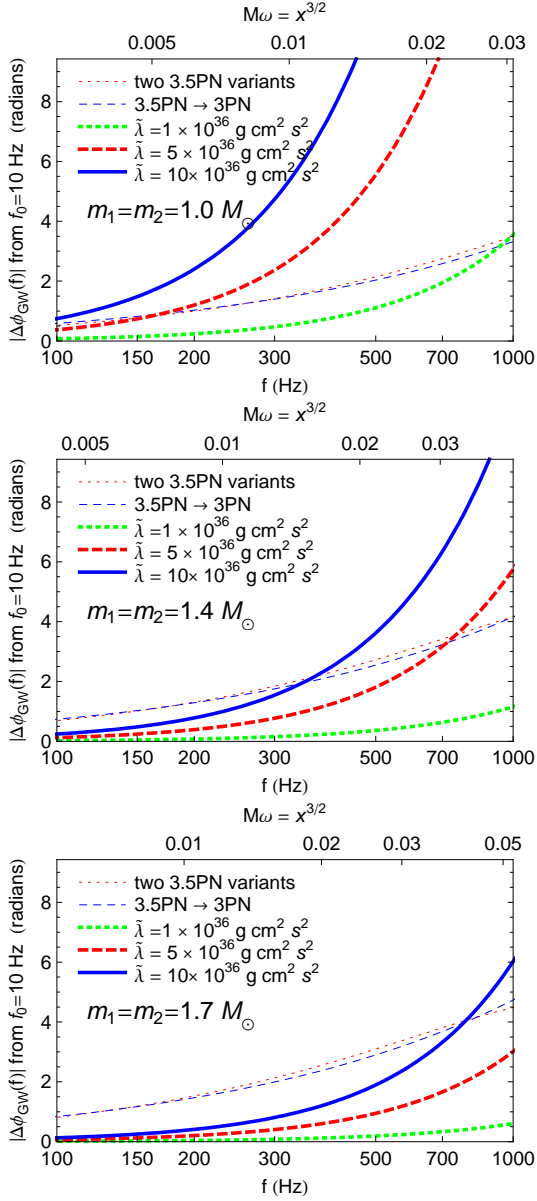


FIG. 4: The reduction in accumulated gravitational wave phase due to tidal effects,  $\Phi_{3.5,PP}(f_{GW}) - \Phi_{3.5,\lambda}(f_{GW})$ , is plotted with thick lines as a function of gravitational wave frequency, for a range of  $\lambda$  appropriate for realistic neutron star EOS and the masses considered. The 3.5 post-Newtonian TaylorT4 PN specification is used as the point-particle reference for the phase calculations. For reference, the difference in accumulated phase between 3.0 and 3.5 post-Newtonian orders of T4 (thin dashed line), and the difference between 3.5 post-Newtonian T4 and 3.5 post-Newtonian T1 (thin dotted line) are also shown. Phase accumulations are integrated from a starting frequency of 10 Hz.

expansions, as well as that from varying the form of the

post-Newtonian Taylor expansion from T4 to T1.<sup>4</sup> An accurate knowledge of the underlying point-particle dynamics will be important to resolve the effects of tidal deformation on the gravitational wave phase evolution at these frequencies.

The half-cycle or more contribution to the gravitational wave phase at relatively low frequencies suggests that this effect could be measurable. Flanagan and Hinderer [11] first calculated the measurability for frequencies below 400 Hz, where the approximations leading to the tidal phase correction are well-justified. We extend the same computation of measurability to a range of masses and mass ratios. We take noise curves from the projected NS-NS optimized Advanced LIGO configuration [44], as well as a proposed noise spectrum of the Einstein Telescope [45]. These noise curves are representative of the anticipated sensitivities of the two detectors. Our results do not change significantly for alternate configurations which have similar sensitivities in the frequency range of interest.

We also extend the computation to a slightly higher cutoff frequency. As estimated in the Appendix, our calculation should still be fairly robust at 450 Hz, as the contributions to the phase evolution from various higher order effects are  $O(10\%)$  of the leading order tidal contribution. The uncertainty in the phase contribution from a given EOS is therefore significantly smaller than the order of magnitude range of phase contributions over the full set of realistic EOS.

The rms uncertainty  $\Delta\tilde{\lambda}$  in the measurement of  $\tilde{\lambda}$  is computed using the standard Fisher matrix formalism [46]. Assuming a strong signal  $h$  and Gaussian detector noise, the signal parameters  $\theta^i$  have probability distribution  $p(\theta^i) \propto \exp(-1/2 \Gamma_{ij} \delta\theta^i \delta\theta^j)$ , where  $\delta\theta^i = \theta^i - \hat{\theta}^i$  is the difference between the parameters and their best-fit values  $\hat{\theta}^i$  and  $\Gamma_{ij} = (\partial h / \partial \theta^i, \partial h / \partial \theta^j)$  is the Fisher information matrix. The parentheses denote the inner product defined in [46]. The rms measurement error in  $\theta^i$  is given by a diagonal element of the inverse Fisher, or covariance, matrix:  $\Delta\theta^i = \sqrt{(\Gamma^{-1})^{ii}}$ .

Using the stationary phase approximation and neglecting post-Newtonian corrections to the amplitude, the Fourier transform of the waveform for spinning point masses is given by  $\tilde{h}(f) = \mathcal{A} f^{-7/6} \exp(i\Psi)$ , where the point-mass contribution to the phase  $\Psi$  is given to 3.5 post-Newtonian order in Ref. [47]. The tidal term

$$\delta\Psi^{\text{tidal}} = -\frac{117\tilde{\lambda}x^{5/2}}{8\eta M^5} \quad (22)$$

Fig. 4 the phase difference between the 3.0PN and 3.5PN

<sup>4</sup> For an explanation of the differences between T4 and T1, see [42, 43].

obtained from Eq. (A.5) adds linearly to this, yielding a phase model with 7 parameters ( $t_c, \phi_c, \mathcal{M}, \eta, \beta, \sigma, \tilde{\lambda}$ ), where  $\beta$  and  $\sigma$  are spin parameters. We incorporate the maximum spin constraint for the NSs by assuming a Gaussian prior for  $\beta$  and  $\sigma$  as in [46]. The uncertainties computed will depend on the choice of point-particle phase evolution, but we assume this to be exactly the 3.5PN form for the current analysis.

The rms measurement uncertainty of  $\tilde{\lambda}$ , along with the uncertainties in chirp mass  $\mathcal{M}$  and dimensionless reduced mass  $\eta$ , are given in Table II and plotted in Figs. 2 and 3, from a single-detector observation of a binary at 100 Mpc distance with amplitude averaged over inclinations and sky positions. If the best-fit  $\tilde{\lambda}$  is zero, this represents a  $1\text{-}\sigma$  upper bound on the physical  $\tilde{\lambda}$ . A signal with best-fit  $\tilde{\lambda} \geq \Delta\tilde{\lambda}$  would allow a measurement rather than a constraint of  $\tilde{\lambda}$ , with  $1\text{-}\sigma$  uncertainty of  $\Delta\tilde{\lambda}$ .

We obtain the following approximate formula for the rms measurement uncertainty  $\Delta\tilde{\lambda}$ , which is accurate to better than 4% for the range of masses  $0.1 M_\odot \leq m_1, m_2 \leq 3.0 M_\odot$  and cutoff frequencies  $400 \text{ Hz} \leq f_{\text{end}} \leq 500 \text{ Hz}$ :

$$\Delta\tilde{\lambda} \approx \alpha \left( \frac{M}{M_\odot} \right)^{2.5} \left( \frac{m_2}{m_1} \right)^{0.1} \left( \frac{f_{\text{end}}}{\text{Hz}} \right)^{-2.2} \left( \frac{D}{100 \text{ Mpc}} \right), \quad (23)$$

where  $\alpha = 1.0 \times 10^{42} \text{ g cm}^2 \text{ s}^2$  for a single Advanced LIGO detector and  $\alpha = 8.4 \times 10^{40} \text{ g cm}^2 \text{ s}^2$  for a single Einstein Telescope detector.

Our results show that the measurability of tidal effects decreases steeply with the total mass of the binary. Estimates of the measurement uncertainty for an equal-mass binary inspiral in a single detector with projected sensitivities of Advanced LIGO and the Einstein Telescope, at a volume-averaged distance of 100 Mpc and using only the portion of the signal between 10 – 450 Hz, are shown in Fig. 2, together with the values of  $\lambda$  predicted by various EOS models. Measurability is less sensitive to mass ratio, as seen in Fig. 3. Comparing the magnitude of the resulting upper bounds on  $\lambda$  with the expected range for realistic EOS, we find that the predicted  $\lambda$  are greatest and the measurement uncertainty  $\Delta\lambda$  is smallest for neutron stars at the low end of the expected mass range for NS-NS inspirals of ( $1 M_\odot - 1.7 M_\odot$ ) [48].

In a single Advanced LIGO detector, only extremely stiff EOS could be constrained with a typical 100 Mpc observation. However, a rare nearby event could allow more interesting constraints, as the uncertainty scales as the distance to the source. Rate estimates for detection of binary neutron stars are often given in terms of a minimum signal-to-noise  $\rho_c = 8$ ; a recent estimate [49] is between 2 and 64 binary neutron star detections per year for a single Advanced LIGO interferometer with a volume averaged range of 187 Mpc. The rate of binaries with a volume averaged distance smaller than 100 Mpc translates to roughly  $(100/187)^3 \simeq 15\%$  of this total detection rate, but over multiple years of observation a rare event could give measurements of  $\tilde{\lambda}$  with uncertainties smaller

than the values in Table II (e.g. with half the tabled uncertainty at 1.9% the total NS-NS rate).

Using information from a network of  $N$  detectors with the same sensitivity decreases the measurement uncertainty by approximately a factor of  $1/\sqrt{N}$  [50], giving more reason for optimism. However, we should also note that, in some ways, our estimates of uncertainty are already too optimistic. First,  $\Delta\lambda$  only represents a 68% confidence in the measurement; a  $2\Delta\lambda$  error bar would give a more reasonable 95% confidence. In addition, our Fisher matrix estimates are likely to somewhat underestimate the measurement uncertainty in real non-Gaussian noise.

In contrast to Advanced LIGO, an Einstein Telescope detector with currently projected noise would be sensitive to tidal effects for typical binaries, using only the signal below 450 Hz at 100 Mpc. The tidal signal in this regime would provide a clean signature of the neutron star core equation of state. However, an accurate understanding of the underlying point-particle phase evolution is still important to confidently distinguish EOS effects.

TABLE II: The rms measurement error in various binary parameters (chirp mass  $\mathcal{M}$ , dimensionless reduced mass  $\eta$ , and weighted average  $\tilde{\lambda}$  of the tidal deformabilities) for a range of total mass  $M$  and mass ratio  $m_2/m_1$ , together with the signal to noise ratio  $\rho$ , using only the information in the portion of the inspiral signal between  $10 \text{ Hz} \leq f \leq 450 \text{ Hz}$ . The distance is set at 100 Mpc, and the amplitude is averaged over sky position and relative inclination.

Advanced LIGO						
$M (M_\odot)$	$m_2/m_1$	$\Delta\mathcal{M}/\mathcal{M}$	$\Delta\eta/\eta$	$\Delta\tilde{\lambda}(10^{36} \text{ g cm}^2 \text{ s}^2)$	$\rho$	
2.0	1.0	0.00028	0.073	8.4	27	
2.8	1.0	0.00037	0.055	19.3	35	
3.4	1.0	0.00046	0.047	31.3	41	
2.0	0.7	0.00026	0.058	8.2	26	
2.8	0.7	0.00027	0.058	18.9	35	
3.4	0.7	0.00028	0.055	30.5	41	
2.8	0.5	0.00037	0.06	17.8	33	
Einstein Telescope						
$M (M_\odot)$	$m_2/m_1$	$\Delta\mathcal{M}/\mathcal{M}$	$\Delta\eta/\eta$	$\Delta\tilde{\lambda}(10^{36} \text{ g cm}^2 \text{ s}^2)$	$\rho$	
2.0	1.0	0.000015	0.0058	0.70	354	
2.8	1.0	0.000021	0.0043	1.60	469	
3.4	1.0	0.000025	0.0038	2.58	552	
2.0	0.7	0.000015	0.0058	0.68	349	
2.8	0.7	0.000021	0.0045	1.56	462	
3.4	0.7	0.000025	0.0038	2.52	543	
2.8	0.5	0.000020	0.0048	1.46	442	

Expected measurement uncertainty will decrease if we can extend the calculation later into the inspiral. From Eq. (23),  $\Delta\tilde{\lambda}$  at 500 Hz is approximately 79% of its value at 450 Hz. The dominant source of error in the tidal phasing at these frequencies are post-Newtonian effects which



scale as  $\lambda x^{7/2}$  and do not depend on any additional EOS parameters. These terms are computed in Ref. [18], and when they are incorporated into the analysis, the resulting phase evolution model can be used at slightly higher frequencies. These terms also add  $\sim 10\%(f/450 \text{ Hz})^{2/3}$  to the strength of the tidal signature.

Higher-order tidal effects and nonlinear hydrodynamic couplings, which depend on unknown NS microphysics, are smaller than post-Newtonian effects by factors of  $\sim x$  and  $\sim x^2$ , so they become important later in the inspiral, where the adiabatic approximation that the mode frequency is large compared to the orbital frequency also breaks down. At this point we can no longer measure only  $\tilde{\lambda}$ , but an EOS-dependent combination of effects including higher multipoles, nonlinearity, and tidal resonances.

However, information in the late inspiral could also constrain the underlying neutron-star EOS. Read et al. [51] estimated potential measurability of EOS effects in the last few orbits of binary inspiral, where the gravitational wave frequency is above 500 Hz, using full numerical simulations. The EOS used for the simulation was systematically varied by shifting the pressure in the core while keeping the crust fixed. The resulting models were parameterized, either by a fiducial pressure or by the radius of the isolated NS model, and measurability in Advanced LIGO was estimated. Such numerical simulations include all the higher order EOS effects described above, but the  $l = 2$  tidal deformability parameter  $\lambda$  should remain the dominant source of EOS-dependent modification of the phase evolution. We therefore expect it to be a better choice for a single parameter to characterize EOS effects on the late inspiral.

The numerically simulated models of [51] can be reparameterized by the  $\lambda$  of the  $1.35 M_{\odot}$  neutron stars considered<sup>5</sup>. The uncertainty of measurement for the new parameter  $\lambda$  can be estimated from Tables II-V of [51]. In the broadband Advanced LIGO configuration of Table IV, it is between 0.3 and  $4 \times 10^{36} \text{ g cm}^2 \text{ s}^2$  for an optimally oriented 100 Mpc binary, or between 0.7 and  $9 \times 10^{36} \text{ g cm}^2 \text{ s}^2$  averaged over sky position and orientation. However, in the NS-NS optimized LIGO configuration of Table III, which is most similar to the Advanced LIGO configuration considered in this paper, the expected measurement uncertainty is more than several times  $\lambda$  for all models. These estimates should be considered order-of-magnitude, as numerical simulation errors are significant, and the discrete sampling of a parameter space allows only a coarse measurability estimate which neglects parameter correlations. In contrast to the perturbative/post-Newtonian estimate of EOS effects calculated in this paper, EOS information in the signal

before the start of numerical simulations is neglected. The estimate is complementary to the measurability below 450 Hz estimated in this paper.

## V. CONCLUSION

We have calculated the relativistic  $l = 2$  Love number  $k_2$  and resulting tidal deformability  $\lambda$  for a wide range of realistic EOS in addition to polytropes. These EOS have tidal deformabilities that differ by up to an order of magnitude in the mass range relevant for binary neutron stars. However, the estimated uncertainty  $\Delta\tilde{\lambda}$  for a binary neutron star inspiral at 100 Mpc using the Advanced LIGO sensitivity below 450 Hz is greater than the largest values of  $\tilde{\lambda}$  except for very low-mass binaries. The uncertainty for the Einstein Telescope, on the other hand, is approximately an order of magnitude smaller than for Advanced LIGO, and a measurement of  $\tilde{\lambda}$  will rule out a significant fraction of the EOS.

Advanced LIGO can place a constraint on the space of possible EOS by obtaining a 95% confidence upper limit of  $\tilde{\lambda}(\mathcal{M}, \eta) \lesssim 2\Delta\tilde{\lambda}(\mathcal{M}, \eta)$ . The tables in Sec. IV can also be scaled as follows: For a network of  $N$  detectors the uncertainty scales roughly as  $\Delta\tilde{\lambda}/\sqrt{N}$ , and for a closer signal we have  $\Delta\tilde{\lambda}(D/100 \text{ Mpc})$ .

## Acknowledgments

We thank S. Hughes, E. Flanagan, and J. Friedman for helpful suggestions and J. Creighton for carefully reading the manuscript. The work was supported in part by NSF Grant PHY-0503366, and by the Deutsche Forschungsgemeinschaft SFB/TR7. TH gratefully acknowledges support from the Sherman Fairchild postdoctoral fellowship, and BL also thanks the Wisconsin Space Grant Consortium fellowship program for support. RNL was supported by NSF Grant PHY-0449884 and the NASA Postdoctoral Program, administered by Oak Ridge Associated Universities through a contract with NASA.

## APPENDIX: ACCURACY OF THE PHASING MODEL

To assess the accuracy of the simple phase evolution model, we compute the corrections to the tidal phase perturbation due to several EOS-dependent effects: the leading order finite mode-frequency terms, higher order tidal effects, and nonlinear hydrodynamic couplings. For simplicity, we will only derive the phase corrections for one star with internal degrees of freedom coupled to a point mass. The terms for the other star simply add. For such a binary system, the Lagrangian can then be

<sup>5</sup> The piecewise polytrope EOS {2H, H, HB, B, 2B} have  $\lambda_{1.35M_{\odot}}$  of {0.588, 1.343, 1.964, 2.828, 10.842}  $\times 10^{36} \text{ g cm}^2 \text{ s}^2$ , respectively.

written as

$$\begin{aligned}
L = & \frac{1}{2}\eta M \dot{r}^2 + \frac{1}{2}\eta M r^2 \dot{\varphi}^2 + \frac{\eta M^2}{r} \\
& - \frac{1}{2}Q_{ij}\mathcal{E}_{ij} + \frac{1}{4\lambda\omega_0^2}\left(\dot{Q}_{ij}\dot{Q}_{ij} - \omega_0^2 Q_{ij}Q_{ij}\right) \\
& - \frac{1}{6}Q_{ijk}\mathcal{E}_{ijk} + \frac{1}{12\lambda_3\omega_{03}^2}\left(\dot{Q}_{ijk}\dot{Q}_{ijk} - \omega_{03}^2 Q_{ijk}Q_{ijk}\right) \\
& - \frac{\alpha}{\lambda^3}Q_{ij}Q_{jk}Q_{ki}. \tag{A.1}
\end{aligned}$$

Here, the star's static mass quadrupole  $Q_{ij}$  parameterizes the  $l = 2$  modes of the star, which can be treated as harmonic oscillators that are driven below their resonant frequency by the companion's tidal field. The tensor  $Q_{ijk}$  parameterizes the star's mass octupole degrees of freedom, and  $\mathcal{E}_{ij}$  and  $\mathcal{E}_{ijk}$  are the  $l = 2$  and  $l = 3$  tidal tensors respectively, which are given by  $\mathcal{E}_{ij} = \partial_i\partial_j(-m_2/r)$  and  $\mathcal{E}_{ijk} = \partial_i\partial_j\partial_k(-m_2/r)$  in Newtonian gravity. The  $l = 3$

deformability constant  $\lambda_3$  is defined by  $Q_{ijk} = -\lambda_3\mathcal{E}_{ijk}$ . The quantities  $\omega_0$  and  $\omega_{03}$  are the  $l = 2$  and  $l = 3$   $f$ -mode frequencies, and  $\alpha$  is a coupling constant for the leading order nonlinear hydrodynamic interactions. In general, one would need to sum over the contributions from all the modes, but other modes contribute negligibly in the regime of interest for the above model (see [52]). Post-Newtonian effects on the Lagrangian for the binary are derived in Ref. [18] and can simply be added to those derived here.

We will be interested in finding an effective description of the dynamics of the system for quasi-circular inspirals in the adiabatic limit, where the radiation reaction timescale is long compared to the orbital timescale. From equilibrium solutions to the Euler-Lagrange equations derived from this Lagrangian, the following radius-frequency relation is obtained:

$$r(\omega) = M^{1/3}\omega^{-2/3}\left[1 + \frac{3\lambda m_2\omega^{10/3}}{M^{5/3}m_1} + \frac{9\lambda m_2\omega^{10/3}}{M^{5/3}m_1}\frac{\omega^2}{\omega_0^2} + \frac{20\lambda_3 m_2\omega^{14/3}}{M^{7/3}m_1} - \frac{18\alpha m_2^2\omega^{16/3}}{M^{8/3}m_1} - \frac{27\lambda^2 m_2^2\omega^{20/3}}{M^{10/3}m_1^2}\right], \tag{A.2}$$

The equilibrium energy, obtained by reversing the signs of the potential energy terms in the Lagrangian, is given by:

$$E = -\frac{1}{2}\eta M^{5/3}\omega^{2/3}\left[1 - \frac{9\lambda m_2\omega^{10/3}}{M^{5/3}m_1} - \frac{45\lambda m_2\omega^{10/3}}{M^{5/3}m_1}\frac{\omega^2}{\omega_0^2} - \frac{65\lambda_3 m_2\omega^{14/3}}{M^{7/3}m_1} + \frac{60\alpha m_2^2\omega^{16/3}}{M^{8/3}m_1} + \frac{63\lambda^2 m_2^2\omega^{20/3}}{M^{10/3}m_1^2}\right]. \tag{A.3}$$

The correction to the energy flux  $\dot{E} = -\frac{1}{5}\langle\ddot{Q}_{ij}^T\ddot{Q}_{ij}^T\rangle$ , where  $Q_{ij}^T = \mu r^2(n^i n^j - \frac{1}{3}\delta_{ij}) + Q_{ij}$  is the total quadrupole moment, is

$$\begin{aligned}
\dot{E} = & -\frac{32}{5}\eta^2 M^{10/3}\omega^{10/3}\left[1 + \frac{6\lambda\omega^{10/3}}{M^{2/3}m_1}\left(2\frac{m_2}{M} + 1\right) + \frac{12\lambda\omega^{10/3}}{M^{2/3}m_1}\frac{\omega^2}{\omega_0^2}\left(3\frac{m_2}{M} + 2\right) + \frac{80\lambda_3 m_2\omega^{14/3}}{M^{7/3}m_1}\right. \\
& \left. - \frac{36\alpha m_2\omega^{16/3}}{M^{5/3}m_1}\left(2\frac{m_2}{M} + 1\right) + \frac{9\lambda^2\omega^{20/3}}{M^{4/3}m_1^2}\left(1 - \frac{2m_2}{M} - \frac{6m_2^2}{M^2}\right)\right]. \tag{A.4}
\end{aligned}$$

Using the formula  $d^2\Psi/d\omega^2 = 2(dE/d\omega)/\dot{E}$  in the stationary phase approximation and integrating twice leads to the final expression for the tidal phase correction:

$$\begin{aligned}
\delta\Psi = & -\frac{9\lambda x^{5/2}}{16\eta M^5}\left(\frac{m_1 + 12m_2}{m_1}\right) - \frac{45\lambda x^{5/2}}{1408\eta M^5}\frac{\omega^2}{\omega_0^2}\left(\frac{8m_1 + 155m_2}{m_1}\right) - \frac{125}{12}\frac{\lambda_3 x^{9/2}}{\eta M^7}\frac{m_2}{m_1} \\
& + \frac{135\alpha m_2 x^{11/2}}{352\eta M^8}\left(\frac{m_1 + 18m_2}{m_1}\right) - \frac{3\lambda^2 x^5}{64\eta M^{10}}\left(\frac{M^2 - 2m_2 M - 83m_2^2}{m_1^2}\right). \tag{A.5}
\end{aligned}$$

We will analyze the information contained in the portion of the signal at frequencies  $f \leq 450$  Hz. This is slightly higher than previously considered, and we now argue that in this frequency band, the simple model of the phase correction is still sufficiently accurate for our purposes. We will evaluate all of the corrections for the case of equal masses  $m_1 = m_2 \equiv m$ . An estimate of the fractional errors for the case of  $m = 1.4 M_\odot$  and

$R = 15$  km is given in parentheses.

1. *Post-1-Newtonian corrections* ( $\sim 10\%$ ).

These corrections give rise to terms  $\propto \lambda x^{7/2}$  that add to those in Eq. (A.5). The explicit form of these terms is computed in Ref. [18] and they depend on the NS physics only via the same parameter  $\lambda$  as the Newtonian tidal terms, so they can easily be incorporated into the data analysis method. Prelimi-

nary estimates indicate that for equal masses, these post-1 Newtonian effects will increase the tidal signal.

2. *Adiabatic approximations* ( $\lesssim 1\%$ ).

The approximation that the radiation reaction time is much longer than the orbital time is extremely accurate, to better than 1%; see Fig. 2 of Ref. [11], which compares the phase error obtained from numerically integrating the equations of motion supplemented with the leading order gravitational wave dissipation terms to that obtained analytically using the adiabatic approximation.

The accuracy of the approximation  $\omega \ll \omega_0$  can be estimated from the fractional correction to (A.5), which is  $\sim (815/1144)(\omega/\omega_0)^2 \sim 0.18(f/f_0)^2$ , where  $f = \omega/\pi$  and  $f_0 = \omega_0/(2\pi)$ . For typical NS models the  $l = 2$   $f$ -mode frequency is [53]

$$\frac{f_0}{\text{kHz}} \approx 0.78 + 1.64 \left( \frac{m}{1.4 M_\odot} \right)^{1/2} \left( \frac{R}{10 \text{ km}} \right)^{-3/2}, \quad (\text{A.6})$$

so that the fractional correction is  $\sim 0.012$  for  $f = 450$  Hz and for a conservatively low  $f$ -mode frequency of  $f_0 = 1700$  Hz.

3. *Higher order tidal effects* ( $\lesssim 0.7\%$ ).

The  $l = 3$  correction to the gravitational wave phase (A.5) is smaller than the  $l = 2$  contribution by a factor of  $\sim (25/351)(k_3/k_2)(m/R)^{-2}x^2 \sim 0.007$ , for  $m/R = 0.14$  and a stiff  $n = 0.5$  polytrope. Here, we have defined the  $l = 3$  Love number  $k_3 = (15/2)\lambda_3 R^{-7}$  and used the values  $k_2 = 0.17$  and  $k_3 = 0.06$  from Ref. [17].

4. *Nonlinear hydrodynamic corrections* ( $\sim 0.1\%$ ).

The leading nonlinear hydrodynamic corrections are characterized by the coupling coefficient  $\alpha/\lambda^3$  in the action. The size of this parameter can be estimated by comparing the Newtonian  $k_2$  to the coupling constants in Lai's ellipsoidal models (e.g. Table 1 of [54]) to be  $\omega^2\alpha/\lambda \sim 2 \times 10^{-3}$ . The nonlinear self-coupling term in Eq. (A.5) is smaller than the leading  $l = 2$  term by a factor  $-285\alpha\omega^2/(572\lambda) \sim 0.001$ .

5. *Spin corrections* ( $\lesssim 0.3\%$ ).

Fractional corrections to the tidal signal due to spin scale as

$$\frac{\delta\Psi_{\text{spin}}}{\delta\Psi_{\text{tidal}}} \propto \left( \frac{\omega_{\text{spin}}}{\omega_{\text{max}}} \right)^2, \quad (\text{A.7})$$

where  $\omega_{\text{max}}$  is the maximum rotational frequency the star can have before breakup, which for most

NS models is  $> 2\pi(1000 \text{ Hz})$ . The observed NS-NS binaries which will merge within a Hubble time have spin periods of  $\sim 23 - 104$  ms, and near the coalescence they will have slowed down due to e.g. magnetic braking, with final spin periods of  $\sim 50 - 130$  ms. The fractional corrections to the tidal signal due to the spin are then  $\lesssim 0.3\%$ .

If the stars have spin, there will also be a spin-induced correction to the phase. As discussed above, the slow-rotation limit is likely to be the relevant regime for our purposes, and using similar methods as for the tidal corrections leads to a phase correction which scales as  $\delta\Psi_s \propto n_2 R^2 / (\eta M^2 x^{1/2}) \omega_{\text{spin}}^2 / (m_1 / R^3)$ , where  $n_2$  is the rotational Love number, which for Newtonian stars is the same as the tidal Love number  $k_2$  and  $\omega_{\text{spin}}$  the spin frequency. The scaling of the spin term as  $\propto x^{-1/2}$  shows that only at large separation do spin effects dominate over tidal effects, which scale as  $\propto x^{5/2}$ .

6. *Nonlinear response to the tidal field* ( $\lesssim 3\%$ ).

We have linearized in  $\lambda$ . Including terms  $\propto \lambda^2$  gives a fractional correction in Eq. (A.5) of  $-(83/7488)k_2 R^5 x^{5/2} / m^5 = -4.8 \times 10^{-11} k_2 (m/M_\odot)^{-10/3} (R/\text{km})^5 (f/\text{Hz})^{5/3} = -0.31 k_2$ .

7. *Viscous dissipation* (negligible).

There have been several analytical and numerical studies of the effect of viscosity during the early part of the inspiral, e.g. [8, 9]. They found that viscous dissipation is negligible during the early inspiral if the volume-averaged shear viscosity  $\eta_{\text{shear}}$  is

$$\eta_{\text{shear}} \lesssim 10^{29} \left( \frac{r}{R} \right)^2 \text{ g cm}^{-1} \text{ s}^{-1}. \quad (\text{A.8})$$

The expected microscopic viscosity of NSs is [55]

$$\eta_{\text{micr}} \sim 10^{22} \left( \frac{\rho}{10^{14} \text{ g cm}^{-3}} \right)^{9/4} \left( \frac{T}{10^6 \text{ K}} \right)^{-2} \text{ g cm}^{-1} \text{ s}^{-1}, \quad (\text{A.9})$$

which is orders of magnitude too small to lead to any significant effect. A variety of other likely sources of viscosity, e. g. the breaking or crumpling of the crust, are also insignificant [8, 9] in the regime of interest to us.

Thus, systematic errors in the measured value of  $\lambda$  due to errors in the model should be  $O(10\%)$ , which is small compared to the current uncertainty of an order of magnitude in  $\lambda$ .

[1] J. M. Lattimer and M. Prakash, Phys. Rep. **442**, 109 (2007), arXiv:astro-ph/0612440.

[2] J. S. Read, B. D. Lackey, B. J. Owen, and J. L. Friedman,

- Phys. Rev. D **79**, 124032 (2009), 0812.2163.
- [3] F. Özel, Nature **441**, 1115 (2006).
- [4] D. A. Leahy, S. M. Morsink, and C. Cadeau, ApJ **672**, 1119 (2008), arXiv:astro-ph/0703287.
- [5] F. Özel, T. Güver, and D. Psaltis, ApJ **693**, 1775 (2009).
- [6] T. Güver, F. Özel, A. Cabrera-Lavers, and P. Wroblewski, ArXiv e-prints (2008), 0811.3979.
- [7] D. A. Leahy, S. M. Morsink, Y. Chung, and Y. Chou, ApJ **691**, 1235 (2009), 0806.0824.
- [8] C. S. Kochanek, ApJ **398**, 234 (1992).
- [9] L. Bildsten and C. Cutler, ApJ **400**, 175 (1992).
- [10] D. Lai and A. G. Wiseman, Phys. Rev. D **54**, 3958 (1996), gr-qc/9609014.
- [11] É. É. Flanagan and T. Hinderer, Phys. Rev. D **77**, 021502 (2008), 0709.1915.
- [12] R. A. Brooker and T. W. Olle, MNRAS **115**, 101 (1955).
- [13] T. Mora and C. M. Will, Phys. Rev. D **69**, 104021 (2004), arXiv:gr-qc/0312082.
- [14] E. Berti, S. Iyer, and C. M. Will, Phys. Rev. D **77**, 024019 (2008), 0709.2589.
- [15] T. Hinderer, ApJ **677**, 1216 (2008), 0711.2420.
- [16] T. Damour and A. Nagar, ArXiv e-prints (2009), 0906.0096.
- [17] T. Binnington and E. Poisson, ArXiv e-prints (2009), 0906.1366.
- [18] É. É. Flanagan and J. E. Vines, in prep. (2009).
- [19] K. S. Thorne and A. Campolattaro, ApJ **149**, 591 (1967).
- [20] T. Regge and J. A. Wheeler, Physical Review **108**, 1063 (1957).
- [21] J. B. Hartle and K. S. Thorne, ApJ **158**, 719 (1969).
- [22] T. Damour and A. Nagar, ArXiv e-prints (2009), 0906.0096.
- [23] M. Lattimer, J.M.; Prakash, The Astrophysical Journal **550**, 426 (2001).
- [24] S. Ransom, P. Demorest, V. Kaspi, R. Ramachandran, and D. Backer, in Binary Radio Pulsars, edited by F. A. Rasio & I. H. Stairs (2005), vol. 328 of Astronomical Society of the Pacific Conference Series, pp. 73–+.
- [25] P. C. C. Freire, A. Wolszczan, M. van den Berg, and J. W. T. Hessels, ApJ **679**, 1433 (2008), 0712.3826.
- [26] D. J. Champion, S. M. Ransom, P. Lazarus, F. Camilo, C. Bassa, V. M. Kaspi, D. J. Nice, P. C. C. Freire, I. H. Stairs, J. van Leeuwen, et al., Science **320**, 1309 (2008), 0805.2396.
- [27] J. P. W. Verbiest, M. Bailes, W. van Straten, G. B. Hobbs, R. T. Edwards, R. N. Manchester, N. D. R. Bhat, J. M. Sarkissian, B. A. Jacoby, and S. R. Kulkarni, ApJ **679**, 675 (2008), 0801.2589.
- [28] P. C. C. Freire, S. M. Ransom, S. Bégin, I. H. Stairs, J. W. T. Hessels, L. H. Frey, and F. Camilo, ApJ **675**, 670 (2008), 0711.0925.
- [29] F. Douchin and P. Haensel, A&A **380**, 151 (2001), arXiv:astro-ph/0111092.
- [30] A. Akmal, V. R. Pandharipande, and D. G. Ravenhall, Phys. Rev. C **58**, 1804 (1998).
- [31] B. Friedman and V. R. Pandharipande, Nuclear Physics A **361**, 502 (1981).
- [32] H. Muther, M. Prakash, and T. L. Ainsworth, Physics Letters B **199**, 469 (1987).
- [33] H. Müller and B. D. Serot, Nuclear Physics A **606**, 508 (1996), arXiv:nucl-th/9603037.
- [34] V. R. Pandharipande and R. A. Smith, Nuclear Physics A **237**, 507 (1975).
- [35] S. Balberg and A. Gal, Nuclear Physics A **625**, 435 (1997), arXiv:nucl-th/9704013.
- [36] N. K. Glendenning, ApJ **293**, 470 (1985).
- [37] B. D. Lackey, M. Nayyar, and B. J. Owen, Phys. Rev. D **73**, 024021 (2006), astro-ph/0507312.
- [38] M. Prakash, J. R. Cooke, and J. M. Lattimer, Phys. Rev. D **52**, 661 (1995).
- [39] M. Alford, M. Braby, M. Paris, and S. Reddy, ApJ **629**, 969 (2005), arXiv:nucl-th/0411016.
- [40] M. Prakash, J. R. Cooke, and J. M. Lattimer, Phys. Rev. D **52**, 661 (1995).
- [41] T. Bulik, D. Gondek-Rosinska, and K. Belczynski, MNRAS **352**, 1372 (2004), arXiv:astro-ph/0310544.
- [42] T. Damour, B. R. Iyer, and B. S. Sathyaprakash, Phys. Rev. D **63**, 044023 (2001), arXiv:gr-qc/0010009.
- [43] M. Boyle, D. A. Brown, L. E. Kidder, A. H. Mroué, H. P. Pfeiffer, M. A. Scheel, G. B. Cook, and S. A. Teukolsky, Phys. Rev. D **76**, 124038 (2007), 0710.0158.
- [44] D. Shoemaker (LSC, 2009), URL <https://dcc.ligo.org/cgi-bin/DocDB/ShowDocument?docid=2974>.
- [45] S. Hild, S. Chelkowski, and A. Freise (2008), arXiv:0810.0604.
- [46] E. Poisson and C. M. Will, Phys. Rev. D **52**, 848 (1995).
- [47] L. Blanchet, Living Reviews in Relativity **9** (2006), URL <http://www.livingreviews.org/lrr-2006-4>.
- [48] I. H. Stairs, Science **304**, 547 (2004).
- [49] R. O’Shaughnessy, V. Kalogera, and K. Belczynski, ArXiv e-prints (2009), 0908.3635.
- [50] C. Cutler and É. É. Flanagan, Phys. Rev. D **49**, 2658 (1994), gr-qc/9402014.
- [51] J. S. Read, C. Markakis, M. Shibata, K. Uryū, J. D. E. Creighton, and J. L. Friedman, Phys. Rev. D **79**, 124033 (2009), 0901.3258.
- [52] É. É. Flanagan and T. Hinderer, Phys. Rev. D **77**, 021502 (2008), 0709.1915.
- [53] K. Kokkotas and B. Schmidt, Living Reviews in Relativity **2**, 2 (1999), arXiv:gr-qc/9909058.
- [54] D. Lai, F. A. Rasio, and S. L. Shapiro, ApJS **88**, 205 (1993).
- [55] C. Cutler and L. Lindblom, ApJ **314**, 234 (1987).